SISSA

Tunable X-ray speckle-based phase-contrast and dark-field imaging using the unified modulated pattern analysis approach

To cite this article: M.-C. Zdora *et al* 2018 *JINST* **13** C05005

View the article online for updates and enhancements.

Related content

IOP e**books**™

Bringing together innovative digital publishing with leading authors from the global scientific community.

Start exploring the collection−download the first chapter of every title for free.

Tunable X-ray speckle-based phase-contrast and dark-field imaging using the unified modulated pattern analysis approach

M.-C. Zdora,[a,b,1] **P. Thibault,**[c] **H. Deyhle,**[c] **J. Vila-Comamala,**[d] **C. Rau**[a,e,f] **and I. Zanette**[a]

[a]*Diamond Light Source, Harwell Science and Innovation Campus,*
Didcot, Oxfordshire, OX11 0DE, United Kingdom

[b]*Department of Physics & Astronomy, University College London,*
London, WC1E 6BT, United Kingdom

[c]*Department of Physics & Astronomy, University of Southampton,*
Southampton SO17 1BJ, United Kingdom

[d]*Institute for Biomedical Engineering, ETH Zürich,*
8092 Zürich, Switzerland

[e]*School of Materials, University of Manchester,*
Manchester M1 7HS, United Kingdom

[f]*Department of Otolaryngology, Northwestern University, Feinberg School of Medicine,*
Chicago, Illinois 60611, U.S.A.

E-mail: marie-christine.zdora@diamond.ac.uk

ABSTRACT: X-ray phase-contrast and dark-field imaging provides valuable, complementary information about the specimen under study. Among the multimodal X-ray imaging methods, X-ray grating interferometry and speckle-based imaging have drawn particular attention, which, however, in their common implementations incur certain limitations that can restrict their range of applications. Recently, the unified modulated pattern analysis (UMPA) approach was proposed to overcome these limitations and combine grating- and speckle-based imaging in a single approach. Here, we demonstrate the multimodal imaging capabilities of UMPA and highlight its tunable character regarding spatial resolution, signal sensitivity and scan time by using different reconstruction parameters.

---

[1]Corresponding author.

Contents

1   Introduction

In the past decades, X-ray multimodal imaging techniques have found increasing applications, in particular for biomedical imaging and material characterisation. The different image modalities can deliver valuable complementary information on the absorption, refraction and small-angle scattering properties of a specimen from a single data set, which are inherently aligned. Among the existing multimodal X-ray imaging techniques, grating interferometry [1, 2] and more recently speckle-based imaging [3, 4] have seen rising interest, in particular as they can also be implemented at laboratory sources with limited spatial and temporal coherence properties [5, 6].

Both of the methods can be employed in either fast single-shot mode, which is limited in spatial resolution, or high-resolution scanning mode, which requires multiple image acquisitions and can be sensitive to beam and setup instabilities. Latest efforts explore more flexible implementations providing a trade-off between the single-shot and scanning modes [7, 8]. The recently proposed unified modulated pattern analysis (UMPA) allows versatile, flexible and tunable multimodal X-ray imaging with a simple arrangement that is easily adapted to specific experimental setups and demands [8]. It is applicable to random as well as periodic reference patterns.

Here, we demonstrate the tunable character of the UMPA approach for accurate, high-contrast multimodal imaging. Using a speckle reference pattern and a sample consisting of different materials, we illustrate the influence of the reconstruction and scan parameters on the differential phase and dark-field images and quantify the image quality in terms of sensitivity and spatial resolution.

2   Experimental setup and image reconstruction

Measurements were conducted at the I13-2 Manchester-Diamond imaging beamline at Diamond Light Source with an X-ray beam of energy 20 keV, extracted from the undulator spectrum with a double-crystal monochromator. The experimental arrangement is illustrated in figure 1. The setup consisted of a diffuser, here two stacked pieces of sandpaper of FEPA granularities P800 and P5000,
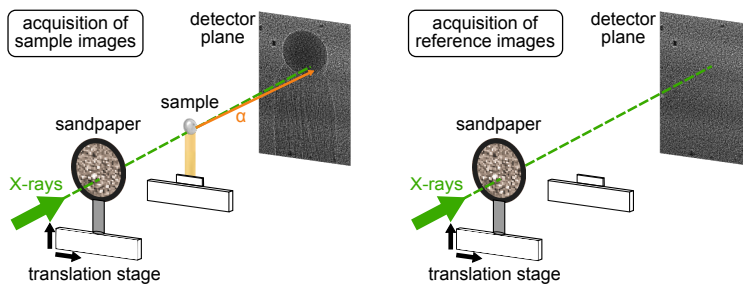
Figure 1. Experimental setup for the UMPA measurements. The diffuser was moved to N different positions and speckle images were recorded with and without the sample in the beam.

the sample mounted on a translation stage 4 cm downstream of the diffuser and a camera system located another $d = 40$ cm downstream. The camera system was a pco.4000 CCD camera (pixel size: 9 μm) coupled to a scintillation screen (250 μm cadmium tungstate), a relay optics system and a 4× magnifying objective lens. This gave an effective detector pixel size of $p_{eff} = 1.12$ μm. The sample was a silicon sphere (diameter: 480 μm) mounted on a wooden toothpick using superglue. For data acquisition with UMPA, the diffuser was moved to several different transverse positions. Images were recorded at each of these positions with and without the sample in the beam.

The scattering and subsequent interference of (partially) coherent X-rays impinging on the diffuser leads to the formation of a random near-field speckle pattern, acting as a wavefront marker. The principle of speckle-based imaging is to analyse the sample-induced modulations of the speckle pattern in position, intensity and visibility to extract a set of multimodal images: the transmission (not further discussed here), the differential phase (refraction), and the dark-field signal [9], which is a measure of small-angle scattering in the sample. In the UMPA formalism, described in detail in ref. [8], the measured interference pattern with the sample in the beam at a diffuser position j is modelled for each pixel (m, n) in terms of the reference interference pattern at the same diffuser position, modulated by the presence of the specimen. In this model, the local transmission $T(m, n)$, dark-field signal $D(m, n)$, and the horizontal and vertical displacement u_x, u_y of the speckle pattern due to refraction are taken into account. A windowed least-squares minimisation routine between the model and the measured intensity with a sum over all N diffuser positions delivers the multimodal signals. The refraction angle signal is given by $(\alpha_x, \alpha_y) = (u_x, u_y) \times p_{eff}/d$ (small-angle approximation). A Fourier phase integration routine [4, 10] was used to combine the information from the horizontal and vertical refraction angle signals to obtain the X-ray phase shift Φ.

3 Phase-contrast and dark-field imaging of a demonstration sample

3.1 Acquired speckle images

Speckle images with and without the sample in the beam were acquired as described in section 2. Figures 2(a) and 2(b) show one of the acquired sample and reference speckle images, respectively, corrected for the dark current of the detector. The visibility of the interference pattern was calculated as the ratio of standard deviation and mean of a 500×500 pixel area in the centre of the reference pattern and is on average 29%. The line profile plots in figures 2(c) and 2(d) through the sample (red) and reference (blue) speckle images demonstrate the modulations of the interference pattern
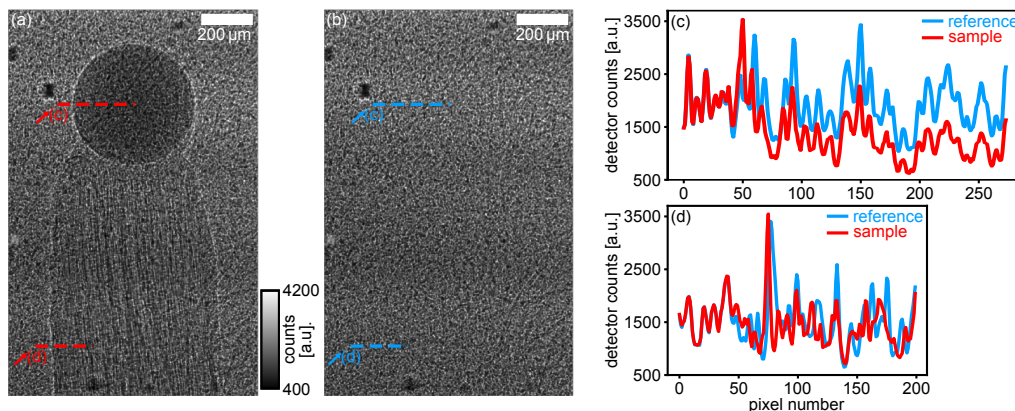
Figure 2. Speckle interference patterns with (a) and without (b) the sample in the beam. Panels (c) and (d) show line plots through the patterns at the positions of the sphere and the toothpick, as indicated in (a), (b).

induced by the silicon sphere, see figure 2(c), and the wooden toothpick, see figure 2(d). On the left side of the plots reference and sample patterns agree almost perfectly, as no sample is present. Inside the sphere a reduction in intensity as well as a displacement of the speckles can be observed in figure 2(c), while the visibility of the speckle pattern is essentially not affected. On the contrary, in figure 2(d) the speckle peaks are broadened and their visibility is strongly reduced due to the scattering nature of the wooden fibres. Furthermore, a slight displacement can be seen, while the change in mean intensity is only subtle as wood is a low absorbing material. It can be observed that a few smaller additional peaks appear in the sample plot, which are due to edge enhancement fringes around the wooden fibres occurring upon free-space propagation.

3.2 Reconstructed multimodal image signals

In the previous section, a displacement and reduction in visibility of the speckle pattern could be observed in areas of the sample. From this information, the refraction angle signals and dark-field small-angle scattering information can be retrieved as described in section 2.

The refraction angle signals α_y in the vertical and α_x in the horizontal direction as well as the phase shift Φ after integration of the two differential signals are shown in figures 3(a), 3(b) and 3(r), respectively, obtained with $N = 20$ steps of the diffuser and an analysis window of size $w \times w = 5 \times 5$ pixels. The expected symmetric refraction behaviour in the two directions of the sphere can clearly be seen. Some uneven features originate from glue on the surface of the sphere.

To demonstrate the tunable character of the UMPA approach, a region of interest of the horizontal refraction α_x centred around the sphere is shown for different reconstruction parameters in figures 3(c)–3(q). The size w of the analysis window and the number N of diffuser steps were varied. The window size sets a limit for the achievable spatial resolution of the reconstructed images [8] and hence a loss in resolution can be observed for increasing w. However, a larger w also improves the angular sensitivity σ, i.e. the sensitivity of the refraction angle measurement [8]. When increasing N at constant w, it can be observed that the spatial resolution is unchanged while the noise level is reduced and there are less artefacts at sharp phase changes such as the edge of the sphere.

The sensitivity values for the different parameter combinations are summarised in table 1. They were determined as the standard deviation in a region of 150×150 pixels in the air background
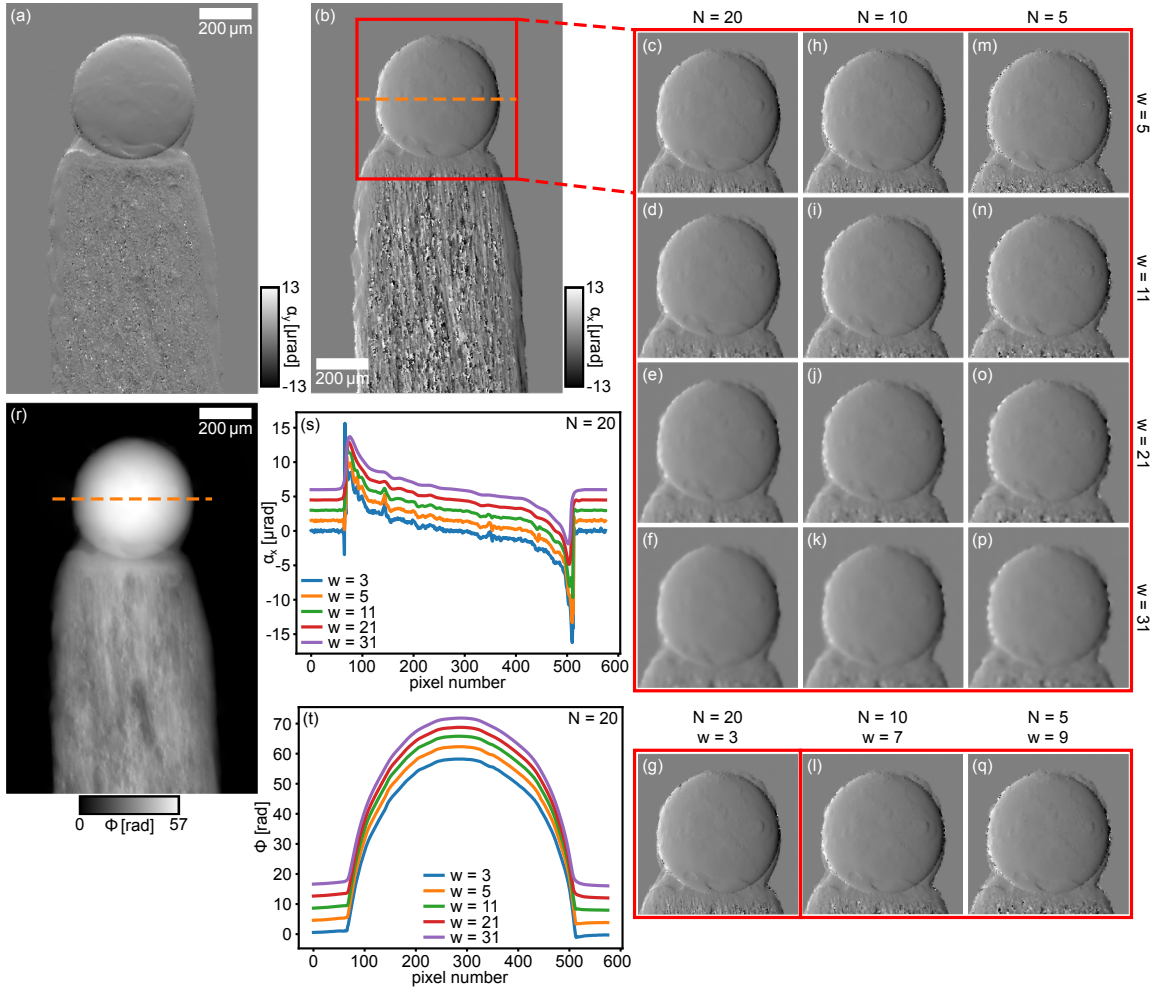
Figure 3. Refraction angles in the vertical (a) and horizontal (b) directions for $N = 20$, $w = 5$. Panels (c)–(q) show the horizontal refraction of the sphere reconstructed for different window sizes w and numbers of steps N. (r) Phase shift integrated from (a), (b). (s), (t) Line plots through the horizontal refraction and integrated phase in the sphere for $N = 20$ and different w. Lines are offset by 1.5 μrad in (s) and 4 rad in (t) for clarity.

Table 1. Angular sensitivity values σ_x, σ_y (in nrad) for the different reconstruction parameters. The parameter combinations that are expected to have similar sensitivity values are highlighted in blue. The first row shows the limit of the spatial resolution in pixels, imposed by the window size.

| Δ [px]	2	4	6	8	10	20	30
w N	**3**	**5**	**7**	**9**	**11**	**21**	**31**
5	-	σ_x 134.6	-	σ_x 50.1	σ_x 34.7	σ_x 12.7	σ_x 7.5
	-	σ_y 185.0	-	σ_y 66.4	σ_y 45.4	σ_y 16.3	σ_y 9.6
10	-	σ_x 93.6	σ_x 55.1	-	σ_x 24.6	σ_x 9.0	σ_x 5.3
	-	σ_y 122.0	σ_y 72.6	-	σ_y 32.6	σ_y 11.7	σ_y 7.1
20	σ_x 112.6	σ_x 64.5	-	-	σ_x 17.6	σ_x 7.0	σ_x 4.4
	σ_y 143.0	σ_y 84.3	-	-	σ_y 25.0	σ_y 11.8	σ_y 9.0

of α_x and α_y. The vertical sensitivity σ_y is reduced compared to σ_x because of the lower vertical coherence of the X-ray beam. The first row of table 1 also gives an indication of the limit Δ in spatial resolution (in pixels), given by twice the full-width-at-half-maximum of the Hamming-type analysis window. If it is desired to decrease N, e.g. for saving time or reducing dose, one should be aware of the decrease in σ for constant w. The angular sensitivity σ is indirectly proportional to the factor $w\sqrt{N}$ [8]. Using this relation, it is possible to determine the required w to achieve the sensitivities as $\sigma_x^{N=20,w=5}$, $\sigma_y^{N=20,w=5}$, but for a reduced N. This gives $w \approx 7$ for $N = 10$ and $w = 10$ for $N = 5$. As uneven window sizes are required, the parameter sets $N = 10$, $w = 7$ and $N = 5$, $w = 9$ were used. The horizontal refraction signals α_x for these settings are shown in figures 3(l) and 3(q) and the corresponding σ values are highlighted in blue in table 1.

Figure 3(g) shows the image with highest resolution at a window size of $w = 3$ with $N = 20$. The higher spatial resolution comes at the cost of a reduced angular sensitivity, see table 1.

In figures 3(s) and 3(t) the horizontal line profiles through the centre of the sphere for the horizontal refraction angle α_x and the integrated phase Φ are plotted for $N = 20$ and the different window sizes w. Note that the curves are shifted vertically by 1.5 µrad in figure 3(s) and 4 rad in figure 3(t) for clarity. The plots demonstrate clearly the gain in angular sensitivity and loss in spatial resolution with increasing window size. From the maximum of the curve in figure 3(t), the phase shift in the centre of the sphere can be estimated, which is measured as $\Phi = 58.4$ rad for $N = 20$, $w = 5$. This compares well with the theoretically expected phase shift of 20 keV X-rays after passing through D = 480 µm of silicon (density: 2.33 g/cm^3): $\Phi = (2\pi/\lambda)\,\delta D \approx 58.9$ rad, where $\lambda_{20\,\text{keV}} = 6.1992 \times 10^{-11}$ m and $\delta_{\text{Si},20\,\text{keV}} = 1.2162 \times 10^{-6}$.

In addition to the refraction signal, the UMPA approach also allows the reconstruction of the dark-field signal, shown in figure 4. As the sphere is made from a single material with homogeneous electron density distribution, only the edges of the sphere and the glue show in the dark-field signal. The wooden fibres of the toothpick, however, lead to strong scattering. The signal intensity increases from the top to the bottom of the toothpick due to the increase in thickness and hence scattering material. As visible in figures 4(b)–4(m), the scatter images show reduced spatial resolution with increasing window size w, as observed for the refraction signal. Furthermore, increased noise for a smaller number N of diffuser steps leads to a more grainy appearance of the dark-field signal.
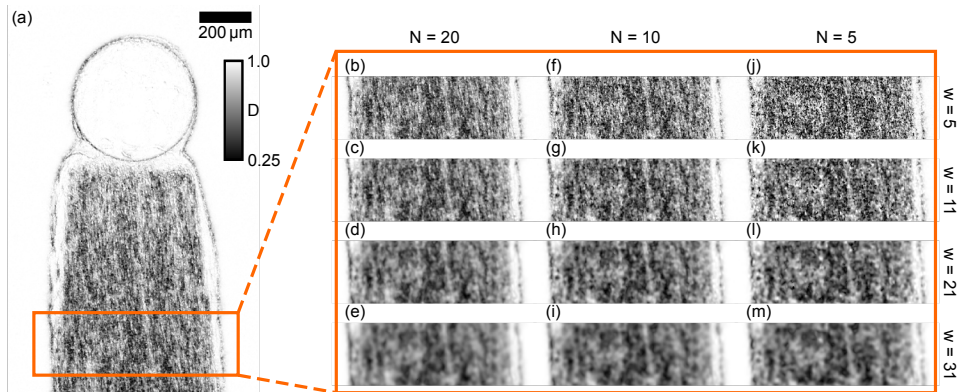
Figure 4. (a) Dark-field signal of the sample obtained with $N = 20$ steps and a window size $w = 5$. (b)–(m) Dark-field signal in a region of interest in the wooden toothpick reconstructed with different parameters.

4 Conclusions and outlook

In this study we have demonstrated the tunable character and potential of the recently proposed UMPA approach for versatile, accurate multimodal X-ray imaging. Using a phantom sample consisting of a silicon sphere and a wooden toothpick, the refraction angle signals in both directions, the integrated phase shift, and the dark-field images were shown for different reconstruction parameters. The expected improvement in angular sensitivity and reduction in noise with increasing number of steps and increasing window size were observed. Moreover, the influence of the window size on the spatial resolution of the images was discussed. The flexibility of the UMPA approach allows adapting the scan and reconstruction parameters to specific experimental requirements, either pushing the spatial resolution with a smaller window size, or keeping a shorter scan time by reducing the number of steps while trading off in resolution. Hence, UMPA bridges the gap between the common single-shot and scanning methods, not only for speckle-based, but also for grating-based imaging, opening new avenues for quantitative, high-contrast multimodal X-ray imaging.

References

[1] A. Momose, S. Kawamoto, I. Koyama, Y. Hamaishi, K. Takai and Y. Suzuki, *Demonstration of x-ray talbot interferometry*, *Jpn. J. Appl. Phys.* **42** (2003) L866.

[2] T. Weitkamp, A. Diaz, C. David, F. Pfeiffer, M. Stampanoni, P. Cloetens et al., *X-ray phase imaging with a grating interferometer*, *Opt. Express* **13** (2005) 6296.

[3] S. Berujon, H. Wang and K. Sawhney, *X-ray multimodal imaging using a random-phase object*, *Phys. Rev.* **A 86** (2012) 063813.

[4] K.S. Morgan, D.M. Paganin and K.K.W. Siu, *X-ray phase imaging with a paper analyzer*, *Appl. Phys. Lett.* **100** (2012) 124102.

[5] F. Pfeiffer, T. Weitkamp, O. Bunk and C. David, *Phase retrieval and differential phase-contrast imaging with low-brilliance x-ray sources*, *Nat. Phys.* **2** (2006) 258.

[6] I. Zanette, T. Zhou, A. Burvall, U. Lundström, D. Larsson, M. Zdora et al., *Speckle-based x-ray phase-contrast and dark-field imaging with a laboratory source*, *Phys. Rev. Lett.* **112** (2014) 253903.

[7] S. Berujon and E. Ziegler, *X-ray multimodal tomography using speckle-vector tracking*, *Phys. Rev. Appl.* **5** (2016) 044014.

[8] M.-C. Zdora, P. Thibault, T. Zhou, F. J. Koch, J. Romell, S. Sala et al., *X-ray phase-contrast imaging and metrology through unified modulated pattern analysis*, *Phys. Rev. Lett.* **118** (2017) 203903.

[9] F. Pfeiffer, M. Bech, O. Bunk, P. Kraft, E. F. Eikenberry, C. Brönnimann et al., *Hard-x-ray dark-field imaging using a grating interferometer*, *Nat. Mater.* **7** (2008) 134.

[10] C. Kottler, C. David, F. Pfeiffer and O. Bunk, *A two-directional approach for grating based differential phase contrast imaging using hard x-rays*, *Opt. Express* **15** (2007) 1175.